ChemCatChem

Research Article
doi.org/10.1002/cctc.202500992

Chemistry Europe
European Chemical Societies Publishing

www.chemcatchem.org

Trends in Oxygen Evolution Reaction Activity and Limiting Steps for Different Active Sites on Co_3O_4(001)

Kapil Dhaka,[a] Stephane Kenmoe,[b] Achim Füngerlings,[c, d] Rossitza Pentcheva,[c, d] Kristina Tschulik,[e, f] and Kai S. Exner*[a, d, f]

Cobalt spinel (Co_3O_4) is a dynamically restructuring catalyst under oxygen evolution reaction (OER) conditions. So far, little is known about the mechanistic complexity of the OER at different active sites of Co_3O_4 at the atomic level. Using the A- and B-terminations of a single-crystal Co_3O_4(001) model electrode, we apply a combination of density functional theory calculations and *ab initio* molecular dynamics simulations to identify three main types of active sites of Co_3O_4 under OER conditions. In addition to tetrahedral and octahedral surface sites, we report the formation of pseudo-octahedral sites due to a change in the local environment upon adsorption of intermediate species. For all these active sites, we analyze the elementary steps of the OER by descriptor-based analysis and the concept of degree of span control. While octahedral and pseudo-octahedral sites are catalytically more active than tetrahedral sites, we show structural sensitivity with respect to the key limiting reaction step, which ranges from O—O bond formation to O_2 desorption and *OH oxidation. Our modeling strategy, which captures changes in the local environment, elementary steps of the OER, and the contribution of different reaction steps to the current density, provides an integrated and comprehensive framework for describing complex oxide materials under applied bias.

1. Introduction

The oxygen evolution reaction (OER) is a key anodic process in electrolyzers to produce clean fuels such as gaseous hydrogen.[1] Despite advances in catalyst design, the OER remains kinetically sluggish due to its complex, multi-electron nature. Overcoming this bottleneck is essential to improving the energy efficiency of water-splitting technologies. Achieving this goal requires not only identifying active materials but also developing a detailed understanding of the atomic-scale factors that control their catalytic performance.

Thermodynamic analysis has been the standard framework for evaluating OER mechanisms[2–5] often through the commonly used thermodynamic overpotential (η_{TD}) as an activity descriptor, which estimates electrocatalytic activity based on the largest free-energy change under equilibrium conditions.[6–9] However, this approach does not account for overpotential and kinetic effects in the analysis of activity trends, nor does it consider that several reaction steps can contribute to a different extent to the reaction rate under operating conditions. OER catalysts, particularly those involving complex oxide surfaces, often reconstruct or undergo chemical transformations under the harsh anodic reaction conditions,[10] thus giving rise to a plethora of different active sites. For such an ensemble of active site motifs, the assumption of a single rate-limiting step oversimplifies the underlying reaction network and may obscure mechanistic competition between different reaction steps and mechanistic pathways.[11,12]

To overcome these limitations, we employ a combined theoretical approach that integrates the potential-dependent free-energy span model of $G_{max}(U)$[13,14] with the degree of span control (DSC) analysis, as introduced recently by Dhaka et al.[11] While the activity descriptor $G_{max}(U)$ identifies the energetically most demanding transition between the intermediate states at a given applied electrode potential, the DSC quantifies how much each individual step for a given mechanism contributes to the current density. This framework enables a more comprehensive evaluation of catalytic performance by not only identifying the thermodynamic bottleneck but also helping to detect situations where more than one reaction step affects the overall reaction rate or where the limiting step changes with increasing overpotential.

[a] K. Dhaka, K. S. Exner
Faculty of Chemistry, Theoretical Catalysis and Electrochemistry, University Duisburg-Essen, Universitätsstraße 5 45141, Essen, Germany
E-mail: kai.exner@uni-due.de

[b] S. Kenmoe
Faculty of Chemistry, Theoretical Chemistry, University of Duisburg-Essen, Universitätsstr. 2 45141, Essen, Germany

[c] A. Füngerlings, R. Pentcheva
Faculty of Physics, Computational Physics of Quantum and Energy, University of Duisburg-Essen, Lotharstr. 1 47057, Duisburg, Germany

[d] A. Füngerlings, R. Pentcheva, K. S. Exner
Center for Nanointegration (CENIDE) Duisburg-Essen 47057, Duisburg, Germany

[e] K. Tschulik
Faculty of Chemistry and Biochemistry, Chair of Analytical Chemistry II, Ruhr University Bochum 44801, Bochum, Germany

[f] K. Tschulik, K. S. Exner
Cluster of Excellence RESOLV 44801, Bochum, Germany

Supporting information for this article is available on the WWW under https://doi.org/10.1002/cctc.202500992

Cobalt oxide (Co_3O_4) has garnered significant attention as an efficient and earth-abundant electrocatalyst for the OER under alkaline conditions.[15] Its favorable electronic structure and multiple oxidation states facilitate key reaction steps in the OER process. Recent studies have shown that tailoring the morphology and introducing defects into Co_3O_4 structures can significantly enhance catalytic performance. For example, laser fragmentation has been used to generate defect-rich Co_3O_4 nanoparticles, resulting in improved activity due to increased surface area and enhanced charge transport.[16] Complementary insights from operando surface X-ray diffraction studies on epitaxial Co_3O_4 thin films have revealed reversible, potential-dependent structural transformations within the topmost atomic layers across a wide pH range, underscoring the dynamic nature of Co_3O_4 surfaces during OER operation.[17,18]

Detailed modeling using the combined approach of $G_{max}(U)$ and DSC becomes especially important in complex electrode materials such as Co_3O_4, where a variety of active sites coexist. Due to its spinel structure, Co_3O_4 exposes multiple types of Co coordination environments on the surface, including tetrahedral and octahedral sites. These coordination geometries offer distinct electronic structures, binding characteristics, and geometric accessibility, which can influence the elementary steps of the OER.[19] Moreover, the nature of the exposed surface itself is sensitive to the electrochemical environment and may undergo dynamic reconstruction or chemical transformations in the presence of water, such as reported in previous works.[20–24] Theoretical studies using *ab initio* molecular dynamics (AIMD) simulations[25–28] revealed that adsorbed water molecules can cause the lifting of surface atoms, leading to new configurations that expose or stabilize previously inaccessible active sites. These reconstructions can modulate the binding of intermediates and thus influence the preferred reaction pathway. A previous study on the Co_3O_4(110) facet also reported surface reconstruction under electrochemical conditions, suggesting that such restructuring of the catalyst, including changes in the local environment, might be a general feature of Co_3O_4 surfaces under OER conditions.[29] Accurately capturing these reconstructed phases is essential for understanding catalytic function under operating conditions, although few mechanistic details are known about the implications of phase reconstruction of Co_3O_4 under anodic polarization on OER activity.[20]

Recent operando surface X-ray diffraction (SXRD) studies have revealed that Co_3O_4 surfaces undergo dynamic reconstruction under OER conditions, forming a reversible cobalt oxyhydroxide ($CoO_x(OH)_y$) layer above approximately 1.15 V versus RHE.[30] This reconstructed skin is proposed to function as an active 3D reaction zone, and, in some cases, has been suggested to revert to the original structure at lower potentials.[31] Moreover, this behavior appears to be intrinsic rather than specific to any particular crystal facet, as similar trends have been observed across various Co_3O_4 orientations and support materials.[20] These experimental insights strongly support the inclusion of non-ideal surface motifs with changes in the local environment—such as pseudo-octahedral Co sites, which were first reported by Bergmann et al. using operando X-ray absorption spectroscopy (XAS),[30] in theoretical models to enable a more realistic representation of catalytic interfaces beyond idealized surface terminations.

In the present manuscript, we investigate the OER on the A- and B- B-terminations of a Co_3O_4(001) model electrode at the single-crystal level, combining AIMD simulations and DFT calculations with appropriate magnetic corrections (cf. Section S3). We model the OER at all symmetry-inequivalent active sites of the A- and B-terminations of Co_3O_4(001) and report the formation of subsurface tetrahedral sites by elevating Co atoms into a pseudo-octahedral position. Our combined framework of the $G_{max}(U)$ and DSC approaches allows us to decipher structure-activity correlations related to the limiting reaction step. Intriguingly, we identify a universal correlation between the coordination of Co and the elementary step that contributes the most to the current density.

2. Theoretical Model

All electronic structure calculations were performed within the framework of density functional theory (DFT) using the Vienna *ab initio* Simulation Package (VASP), augmented with the implicit solvation model implemented in the VASPsol extension.[32–35] Detailed computational parameters, including the choice of exchange-correlation functional, plane-wave cutoffs, k-point sampling, and convergence criteria, are provided in Section S1.

The oxygen evolution reaction (OER) involves the transfer of four proton-electron pairs under the formation of an O—O bond. This makes it a kinetically and thermodynamically demanding process that only occurs under harsh anodic conditions, and relevant current densities in the order of several mA/cm^2 are only achieved for $U > 1.50$ V versus RHE (reversible hydrogen electrode)[36–39] (where U refers to the applied electrode potential; we adopt this notation to distinguish it from the total energy, E, in DFT calculations). To capture the elementary steps of the OER at the atomic level, we analyzed multiple possible mechanistic pathways for the OER, including mononuclear, bifunctional, binuclear, and concerted Walden-type mechanisms.[40–42] Details of the different OER mechanisms considered in this study can be found in Section S2.

It is important to emphasize that our DFT-based model describes OER activity under idealized interfacial conditions and moderate current densities (~10 mA cm^{-2}), as typically used in laboratory-scale studies. These current densities correspond to overpotentials in the range of about 300–400 mV. In contrast, industrial electrolyzers operate at much higher current densities (≥500 mA cm^{-2}, up to 1–2 A cm^{-2}), where macroscopic effects such as bubble formation, mass transport limitations, and local heating become dominant. Such phenomena are not accessible within the framework of static DFT and the computational hydrogen electrode (CHE) approach applied here,[43] although certain local dynamical effects can be addressed using molecular dynamics (MD) simulations. Therefore, the current study focuses on atomistic insights into structure–activity trends rather than

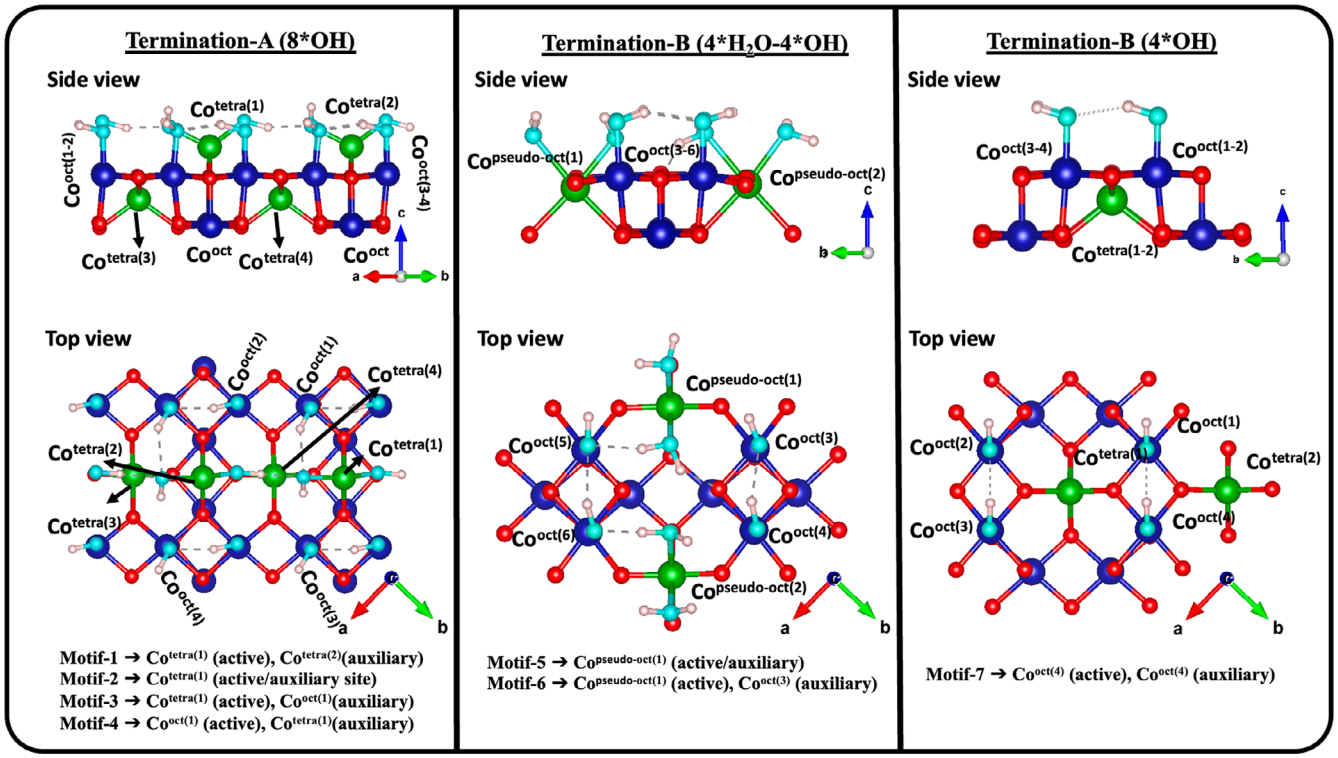

Figure 1. Schematic representation of various surface configurations of Co_3O_4(001), including termination-A (8*OH coverage) and termination-B (4*H_2O-4*OH and 4*OH coverages). All seven structural motifs considered for OER are illustrated. Blue and red spheres denote Co atoms in octahedral coordination and lattice oxygen atoms, respectively. Green spheres indicate tetrahedral Co atoms, including those that transition to pseudo-octahedral coordination, while cyan spheres represent surface-adsorbed oxygen atoms. White color represents hydrogen atoms. Please note that the atom sizes do not scale.

on predicting catalyst performance under industrial operating conditions.

In the following, we provide a detailed structural analysis of the different active site motifs on the Co_3O_4 surface under OER conditions.

2.1. Surface Models

Previous theoretical work[11] has shown that the surface of Co_3O_4 is hydroxylated under typical OER conditions of $U > 1.23$ V versus RHE, which is in qualitative agreement with former works by Peng et al.[6] and Hajiyani et al.[44] This is the reason why our surface models are *OH-covered at the different Co active sites. Pourbaix diagrams for the A- and B-terminations of the Co_3O_4(001) surface are discussed in Section S3 and confirm the stability of *OH/ *OH_2-capped surface configurations under OER conditions.

Figure 1 illustrates seven structurally distinct motifs identified at the A- and B-terminations of the Co_3O_4(001) surface, comprising four configurations derived from termination-A and three from termination-B. These motifs are systematically analyzed to explore the influence of local atomic arrangements on OER activity, with particular emphasis on tetrahedral (Co^{tetra}) and octahedral (Co^{octa}) coordination environments. Please note that in addition to the main active site, we also include auxiliary sites, since some of the OER mechanisms (cf. Section S2) require a second site for the formation of O_2.

Motif-1 represents a configuration on termination-A in which two surface Co^{tetra} sites are separated by approximately 5.65 Å. While both sites are geometrically accessible, the large distance between them renders cooperative or bifunctional reaction pathways requiring a second active (auxiliary) site challenging.

In **Motif-2**, both the active and auxiliary sites are Co^{tetra}. Therefore, this configuration allows us to probe the catalytic behavior of tetrahedral Co sites as the main active center.

Motif-3 features a Co^{tetra} atom as the primary active site, with a subsurface Co^{oct} atom serving as the auxiliary site. This vertical coupling introduces a mixed coordination environment that can influence intermediate stabilization and electron transfer by considering the importance of sublayer interactions in determining reactivity.

Motif-4 is an inversion of **Motif-3**, where the active site on the surface is a Co^{oct} atom (as commonly found in termination-B), but the auxiliary site is a Co^{tetra} atom. This hybrid configuration bridges the structural characteristics of terminations A and B and provides insights into how Co^{tetra} involvement can alter activity in a termination-B-like environment.

We performed *ab initio* molecular dynamics simulations for the A termination of Co_3O_4(001) to verify whether the atomic arrangement of these active sites is stable upon contact with water.[45] We refer to Section S3 for details (cf. Figure S2). As further explained in this section, the subsurface Co^{tetra} sites of the B termination tend to change their coordination under OER conditions upon contact with water: the Co^{tetra} atoms lift into the solvent interface and transform into six-fold coordi-

nated species due to hydration (cf. Figures S3 and S4 in Section S3) by neutral water molecules (pH ~7). Therefore, the original Co^{tetra} sites become pseudo-octahedral sites and are available for OER. We note that this type of reconstruction significantly modifies the local coordination geometry and electronic environment, and similar changes in the local environment have been reported in previous studies on the A-termination of Co_3O_4(001).[6,44]

In **Motif-5**, the $Co^{pseudo\text{-}oct}$ site, formed by the lifting and re-coordination of a formerly tetrahedral subsurface Co atom under anodic polarization, serves both as the active site and the auxiliary site. In contrast, **Motif-6** separates these roles: the lifted $Co^{pseudo\text{-}oct}$ site functions as the primary active center, while a nearby octahedral Co atom on the surface acts as the auxiliary site.

Motif-7 represents the conventional configuration on termination-B, in which adjacent surface Co^{oct} atoms fulfill both the active and auxiliary functions. This widely studied arrangement acts as a reference point for evaluating the performance of alternative motif architectures, particularly considering that experimental work on the OER over Co_3O_4 suggested that the active Co sites reveal an octahedral coordination.[46,47] Note that a detailed discussion of the elementary reaction steps in the OER on **Motif-7** is also available in a previous work by Dhaka and Exner.[11]

In the following, we discuss the mechanistic and energetic implications of the seven different Co sites on OER activity. This comparative approach allows us to identify key structural factors that promote efficient catalysis by distinguishing between tetrahedral, octahedral, and pseudo-octahedral coordination.

3. Results and Discussion

3.1. OER Mechanism on Different Active Site Motifs of Co_3O_4(001)

To systematically evaluate the catalytic behavior of Co_3O_4(001) under OER conditions, we investigated several mechanistic pathways, as detailed in Section S2. These include mononuclear, bifunctional, binuclear, oxide, and Walden-type mechanisms, capturing a broad range of plausible reaction channels on the surface. The relative activity of each mechanism was assessed using the activity descriptor $G_{max}(U)$,[13,14] which is a potential-dependent activity descriptor based on the energetic span model.[48] This quantity reflects the largest free-energy difference between any two intermediate states in a given pathway and provides a measure of the electrocatalytic activity: a lower $G_{max}(U)$ indicates a more favorable mechanism.

It is important to note that the OER can proceed via different reaction channels depending on the pH of the electrolyte:

$$\text{In alkaline conditions}: \; 4OH^- \rightarrow O_2 + 2H_2O + 4e^-$$

$$\text{In acidic conditions}: \; 2H_2O \rightarrow O_2 + 4H^+ + 4e^-$$

These routes differ in the reactant and can therefore also exhibit different kinetics with regard to adsorption, desorption, and surface reactions. In the present work, we do not differentiate between them. Our analysis is based on the CHE approach, which assumes a Nernstian potential shift with increasing pH and thus does not explicitly capture pH or electrolyte-specific effects. To resolve these effects, grand-canonical DFT calculations[49] at constant electrode potential are required, which are beyond the scope of the present work.

We are aware that the majority of computational works apply the thermodynamic overpotential, η_{TD}, as the activity descriptor to render predictions on the electrocatalytic activity.[50] Although it would be helpful to compare the energetics obtained in the present paper with those of previous works,[6,15,44,51] we note that the concept of η_{TD} neither allows the description of chemical steps in the activity analysis nor enables the determination of the contribution of several elementary steps to the reaction rate via the concept of the degree of span control.[11] To this end, we report the free-energy changes for all reaction mechanisms considered in our analysis in Section S4 (cf. Tables S1–S7) and discuss activity trends using the $G_{max}(U)$ descriptor in the main text of our work.

To determine the $G_{max}(U)$ descriptor, we construct free-energy diagrams along the reaction coordinate for all mechanistic pathways as a function of the seven structural motifs considered (cf. Figure 1) at an applied potential of $U = 1.53$ V versus RHE; note that an applied overpotential of at least 300 mV is typically required on the anode side to reach current densities in the order of 10–100 mA/cm^2.[52] Our results are summarized in Table 1, where $G_{max}(U)$ values for all surface motifs of termination-A and termination-B of Co_3O_4(001) are given. Figure 2 depicts the free-energy landscapes for the different OER mechanisms of the tetrahedral sites of **Motif-1** and **Motif-2**. The free-energy diagrams for **Motif-3** to **Motif-7** are compiled in Figures S5 and S6 of Section S4.

Among the seven motifs, the global minimum for the $G_{max}(U)$ descriptor is 0.00 eV at $U = 1.53$ V vs. RHE (cf. Table 1). To avoid ambiguities in the selection of favorable reaction pathways, we adopt a cutoff of $G_{max}(U = 1.53\text{ V vs. RHE}) < 0.25$ eV. This cutoff is inspired by the sensitivity of the $G_{max}(U)$ descriptor, which is reported to be on the order of 0.20 eV:[14] only if the value of $G_{max}(U)$ for two different mechanisms differs by at least 0.20 eV, we conclude that the pathway with the smaller $G_{max}(U)$ value is energetically preferred. Therefore, all mechanisms that fall into this range are considered relevant and lead to highly active sites, allowing a consistent comparison across structurally different active site environments.

Among the seven motifs evaluated, **Motif-1**, **Motif-2** (cf. Figure 2), and **Motif-3** (cf. Figure S5) feature tetrahedral coordination and display a wide range of catalytic behavior in terms of OER activity. **Motif-2** clearly stands out as the most active site, and it facilitates O_2 formation by three mechanisms with a low $G_{max}(U = 1.53\text{ V})$ value, namely bifunctional-II (0.13 eV), bifunctional-Walden (0.19 eV), and binuclear (0.23 eV). This indicates that **Motif-2** offers multiple thermodynamically accessible pathways for OER and facilitates the formation of molecular oxygen through multiple mechanisms.

Table 1. $G_{max}(U)$ values as a measure for the electrocatalytic activity at $U = 1.53$ V versus RHE for seven different OER mechanisms on the different active site motifs of termination-A and B of $Co_3O_4(001)$ (cf. Figure 1). Values highlighted in blue represent the most favorable mechanism(s) based on the $G_{max}(U)$ analysis for each motif, including all pathways with $G_{max}(U = 1.53$ V vs. RHE$) < 0.25$ eV.

	$G_{max}(U)$ (eV) at $U = 1.53$ V vs RHE						
	Motif-1	Motif-2	Motif-3	Motif-4	Motif-5	Motif-6	Motif-7
Mononuclear	0.32	0.32	0.32	0.60	0.60	0.60	**0.08**
Mononuclear-Walden	0.31	0.31	0.31	0.61	**0.24**	**0.15**	**0.09**
Bifunctional-I	0.57	0.39	0.37	0.42	0.53	0.48	0.36
Bifunctional-Walden	0.42	**0.19**	0.61	**0.12**	**0.00**	**0.13**	**0.08**
Bifunctional-II	0.41	**0.13**	**0.24**	**0.11**	0.70	1.13	**0.22**
Binuclear	0.59	**0.23**	0.30	0.61	1.33	0.47	0.52
Oxide	1.48	1.33	1.02	1.02	1.44	1.48	0.20

In contrast, **Motif-1** exhibits significantly higher values of the $G_{max}(U)$ descriptor across all mechanisms, with the lowest $G_{max}(U)$ value being 0.31 eV for the mononuclear-Walden pathway. We relate this poor catalytic performance in the OER to the large separation between the active and auxiliary Co sites, as discussed in Section 2 (cf. Figure 1). As a result, bifunctional and binuclear mechanisms requiring two major active sites are geometrically inaccessible, and only less efficient single-site pathways such as the mononuclear mechanism remain. The OER activity of **Motif-3** is moderate, considering that the bifunctional-II and binuclear mechanisms show $G_{max}(U)$ of 0.24 and 0.30 eV, respectively. Overall, this comparison shows that among the tetrahedral motifs, only **Motif-2** provides the spatial and energetic conditions required for efficient OER catalysis.

Octahedral sites, represented by **Motif-4** (Figure S5) and **Motif-7** (Figure S6), exhibit greater mechanistic flexibility and consistently favorable energetics compared to their tetrahedral counterparts. **Motif-7** has the lowest $G_{max}(U)$ values among these two motifs, with 0.08 eV for both the mononuclear and bifunctional-Walden mechanisms and 0.09 eV for the mononuclear-Walden description. In comparison, **Motif-4** catalyzes the OER mainly via bifunctional pathways with $G_{max}(U)$ values of 0.11 eV or 0.12 eV. Considering the slight differences in energetics between motifs 4 and 7, it can be concluded that **Motif-4** is similarly active in the OER as **Motif-7**. The ability of both octahedral motifs to support multiple reaction pathways underlines their catalytic relevance under OER conditions.

Pseudo-octahedral motifs, represented by **Motif-5** and **Motif-6** in Figure S6, also show promising OER activity, but with higher mechanistic selectivity. **Motif-5** yields the global minimum among the motifs considered, with a $G_{max}(U)$ value of 0.00 eV for the bifunctional-Walden mechanism. Considering the sensitivity of the $G_{max}(U)$ descriptor,[14] no other mechanism is clearly favored on this pseudo-octahedral site. Since we used $G_{max}(U = 1.53$ V versus RHE$) < 0.25$ eV in Table 1 to differentiate between active and inactive pathways, there is a certain propensity for the mononuclear-Walden with a $G_{max}(U)$ value of 0.24 eV. **Motif-6** is slightly less active than **Motif-5**, although the $G_{max}(U)$ values for the bifunctional-Walden and mononuclear-Walden mechanisms of 0.13 and 0.15 eV, respectively, indicate that this pseudo-octahedral site is also sufficiently active in the OER. These results stress that pseudo-octahedral motifs, which form due to surface reconstruction under anodic polarization, where Co atoms originally in tetrahedral coordination are elevated into near-octahedral positions, represent relevant active sites that compete with octahedral sites in terms of OER activity.

Overall, both octahedral and pseudo-octahedral sites prove to be similarly active and offer multiple mechanistic pathways with $G_{max}(U)$ values below the chosen threshold of $G_{max}(U = 1.53$ V versus RHE$) < 0.25$ eV to distinguish between active and inactive motifs. Tetrahedral sites are still catalytically somewhat active but are more often outside the range of high OER activity. This indicates a slightly lower intrinsic activity of the tetrahedral sites compared to their octahedral counterparts. Nonetheless, all three site types contribute to the catalytic activity of the OER on the $Co_3O_4(001)$ surface. The coexistence of multiple active site geometries and the associated mechanistic preferences underline the importance of structural diversity, not only for controlling the dominant OER pathway but also for maximizing catalytic efficiency through complementary reactivity. This understanding could provide a valuable framework for rational catalyst design in the future, where fine-tuning the distribution and accessibility of specific surface motifs can improve the overall OER performance.

3.2. Identifying Limiting Steps by the Degree of Span Control

Electrocatalytic studies often use the approximation that the overall reaction rate is governed by a single elementary step, which is called the rate-determining step (RDS).[53] When using DFT calculations to identify the limiting step in the mechanistic cycle, the RDS is typically approximated by determining the potential-determining step (PDS), taking into account that the calculation of transition states in an electrochemical environment is computationally intensive and often imprecise.[54–56] While the assumption of a single rate-determining step simplifies the complex nature of electrocatalytic processes, multiple steps can collectively influence the rate, especially under conditions where multiple reaction mechanisms are operative. For example, a shift in the Tafel slope is often attributed to a change in RDS,

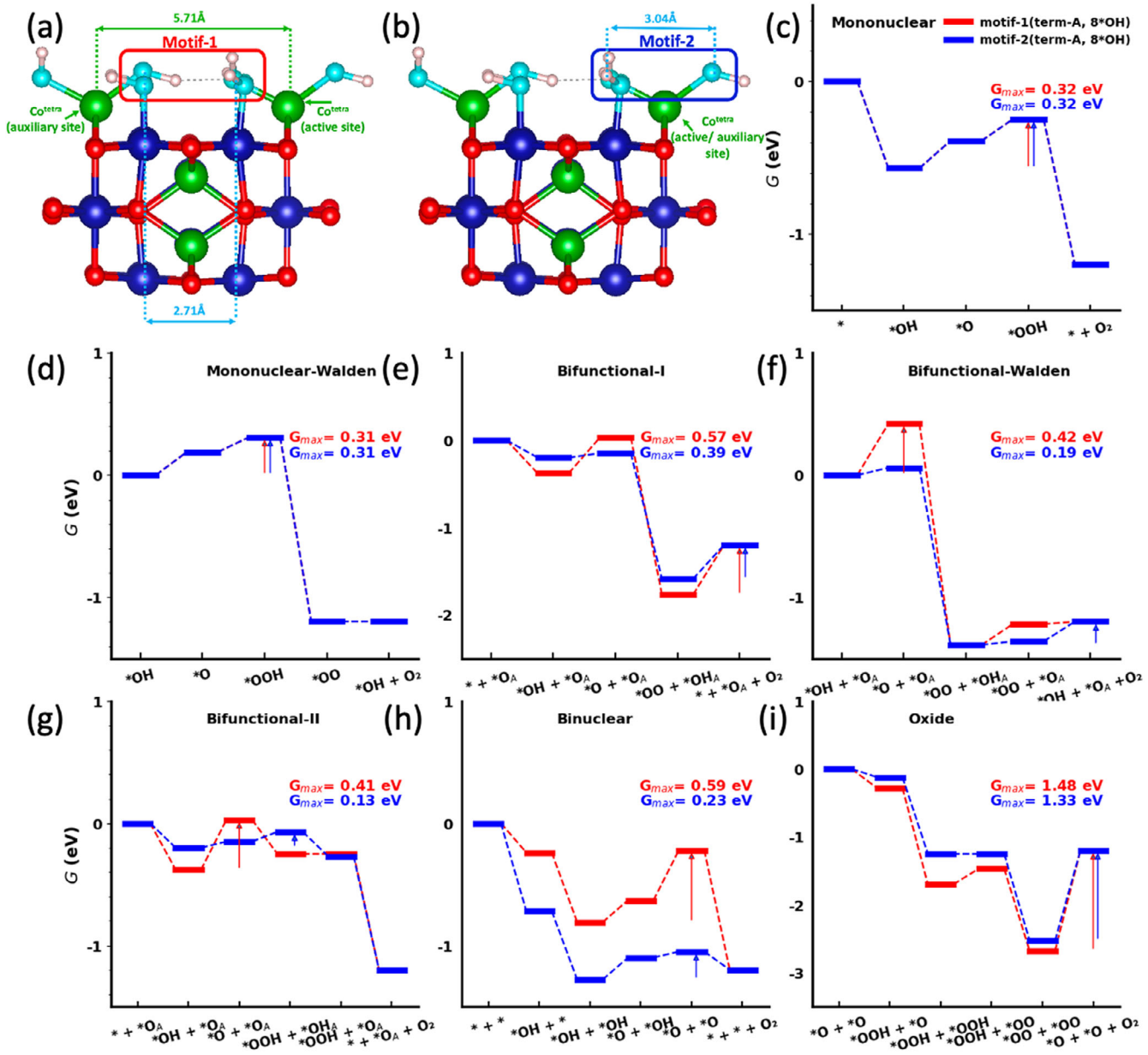

Figure 2. Free-energy diagram of seven OER mechanisms on the Co_3O_4(001)-8*OH surface of termination-A at $U = 1.53$ V versus RHE. **Motif-1** (red) and **Motif-2** (blue), shown in panels (a) and (b), represent two distinct catalytic configurations characterized by different arrangements of active and auxiliar Co sites with different separations. Panels (c–i) illustrate the free-energy profiles for the mononuclear, mononuclear-Walden, bifunctional-I, bifunctional-Walden, bifunctional-II, binuclear, and oxide mechanisms, respectively. For each pathway and motif, the $G_{max}(U = 1.53$ V versus RHE) values are indicated by an arrow. All pathways with $G_{max}(U = 1.53$ V versus RHE) < 0.25 eV are considered highly active in OER.

although previous works on this topic reported a more nuanced understanding of these shifts by applying the concept of the generalized degree of rate control.[57–59] This framework, introduced by Campbell to study thermal catalytic reactions, goes beyond the concept of a single RDS by considering that multiple elementary steps can contribute to the reaction rate to a different extent.[60,61]

If the transition states for all seven reaction pathways investigated for the different active sites in Section 3.1 were known, it would be a straightforward task to determine the generalized degree of rate control and to draw conclusions about the limiting reaction steps based on a rigorous kinetic analysis. Unfortunately, the theoretical electrochemistry community has not yet reached this point, and the calculation of transition states often relies on chemical reaction steps rather than steps involving charge transfer.[56,62,63] To overcome this caveat, Dhaka et al. recently introduced the concept of the degree of span control (DSC),[11] which can be viewed as a thermodynamic representation of the generalized degree of rate control based on the application of the $G_{max}(U)$ descriptor. Using the DSC approach, we can track the contribution of the different reaction steps within the seven mechanisms to the OER rate as a function of the applied electrode potential for all active site motifs considered in this work. Details for the application of this framework are

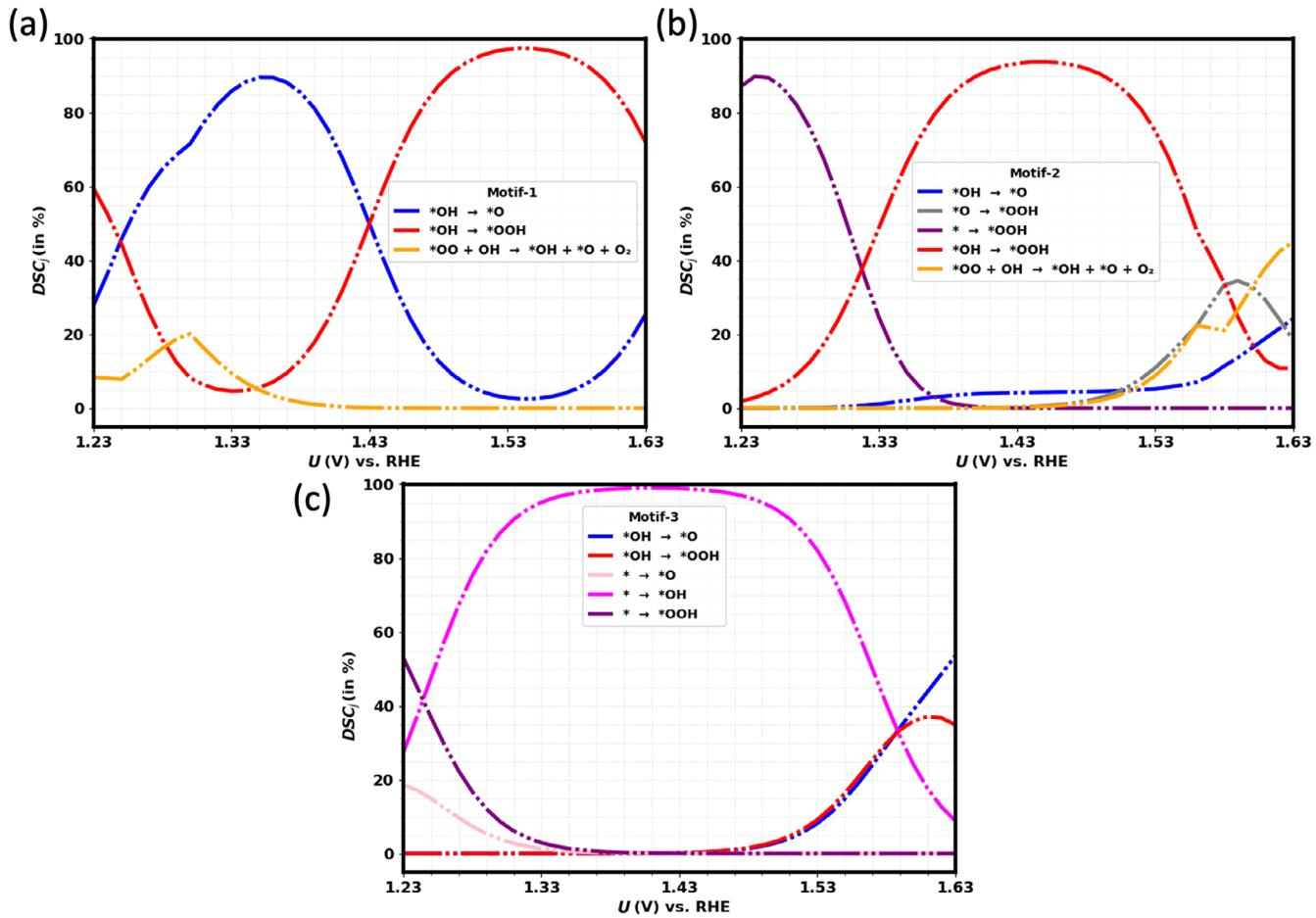

Figure 3. Potential-dependent degree of span control (DSC_j) for the elementary steps of the OER on the tetrahedral motifs of $Co_3O_4(001)$ (see Figure 1): a) **Motif-1**, b) **Motif-2**, and c) **Motif-3**. Contributions below 5% are excluded for clarity. The analysis reveals that the main limiting steps across the different tetrahedral motifs include * → *OH, *OH → *O, *O → *OOH, *OH → *OOH, and *OO + *OH → *OH + *O + O_2, highlighting the critical role of *OH formation, *OH oxidation, O—O bond formation and O_2 desorption through a Walden-like step in the OER, respectively.

summarized in Section S5. There, we also resolve the contribution of the different reaction mechanisms to the current density for each motif (cf. Figures S7–S9).

Figures 3, 4, and 5 present the potential-dependent degree of span control (DSC_j) for the oxygen evolution reaction across three key structural motifs of $Co_3O_4(001)$, namely tetrahedral, pseudo-octahedral, and octahedral sites, respectively. These motifs, defined by their distinct cobalt coordination environments, exhibit different mechanistic bottlenecks that determine the reaction rate of the OER, and a structure-activity relationship emerges that is consistent for all motifs considered.

For the tetrahedral motifs (**Motif-1–3**, cf. Figure 3), the DSC analysis consistently identifies the formation of the *OOH intermediate as the dominant limiting step. While in **Motif-1,** the oxidation of the *OH adsorbate is governing the reaction rate for $U > 1.40$ V versus RHE, *OOH formation becomes limiting for larger anodic overpotentials, with a contribution to the reaction rate between 50% and 100% depending on applied bias. We note that the oscillating DSC behavior in **Motif-1** reflects an internal switching between the different limiting steps due to the involvement of different sites in an overall less active motif. A slightly different, yet qualitatively comparable picture is observed for **Motif-2**. There, different spans giving rise to *OOH formation are identified as the main kinetic bottleneck for $U < 1.60$ V versus RHE (with a contribution to the reaction rate close to 100%), and only at larger anodic overpotentials is the desorption of O_2 through a Walden-like step the main limitation of the catalytic activity. **Motif-3** is not a classical tetrahedral motif, considering that this site consists of a vertical coupling with a subsurface Co^{oct} serving as an auxiliary site (cf. Figure 1). This can be seen as the main reason why the DSC_j plot for **Motif-3** differs from the other two sites. In this case, the formation of *OH is the main limiting step for potentials up to 1.55 V versus RHE, although the formation of the *OOH adsorbate becomes relevant with a contribution of almost 40% at $U = 1.60$ V versus RHE. Based on Figure 3c, the main limiting step under these potential conditions is related to the oxidation of the *OH intermediate, which we trace to the presence of the octahedral auxiliary site: the transformation of *OH to *O takes place in bifunctional pathways on the octahedral auxiliary site rather than the tetrahedral site, and bifunctional mechanisms are preferred for **Motif-3** (cf. Figure S7 in Section S5). Therefore, the limiting step for the tetrahedral site of **Motif-3** is indeed the formation of the *OOH adsorbate for sufficiently large anodic

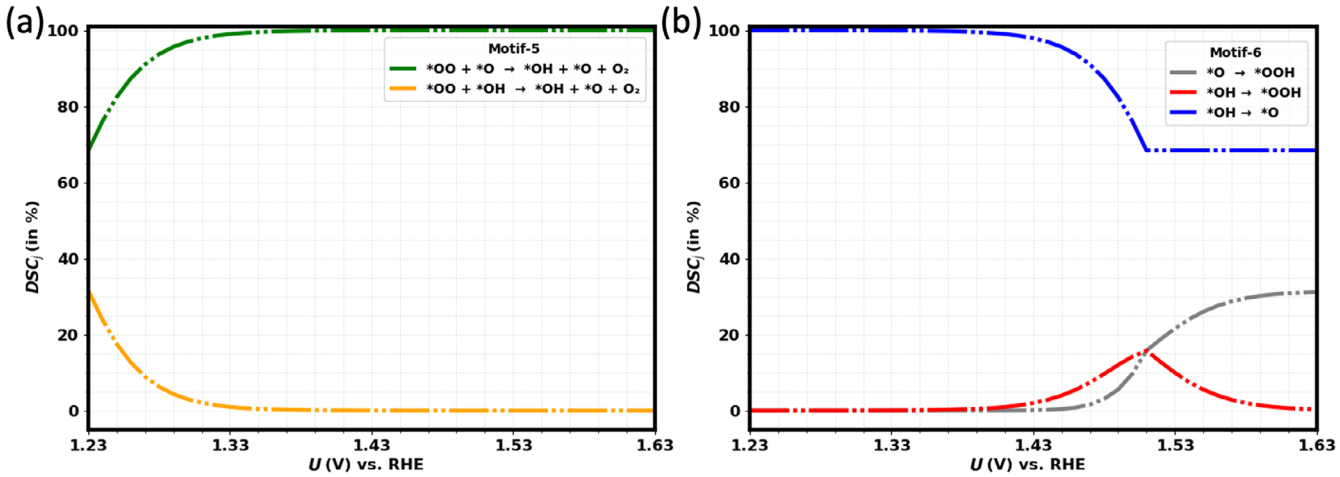

Figure 4. Potential-dependent degree of span control (DSC_j) for the elementary steps of the OER on the pseudo-octahedral motifs of Co_3O_4(001) (see Figure 1): a) **Motif-5**, b) **Motif-6**. Contributions below 5% are excluded for clarity. In **Motif-5**, the reaction is consistently limited by the concerted desorption-adsorption step of oxygen and water (*OO + *O → *OH + *O + O_2), while in **Motif-6** the elementary step of *OH oxidation at the octahedral auxiliary site governs the electrocatalytic activity.

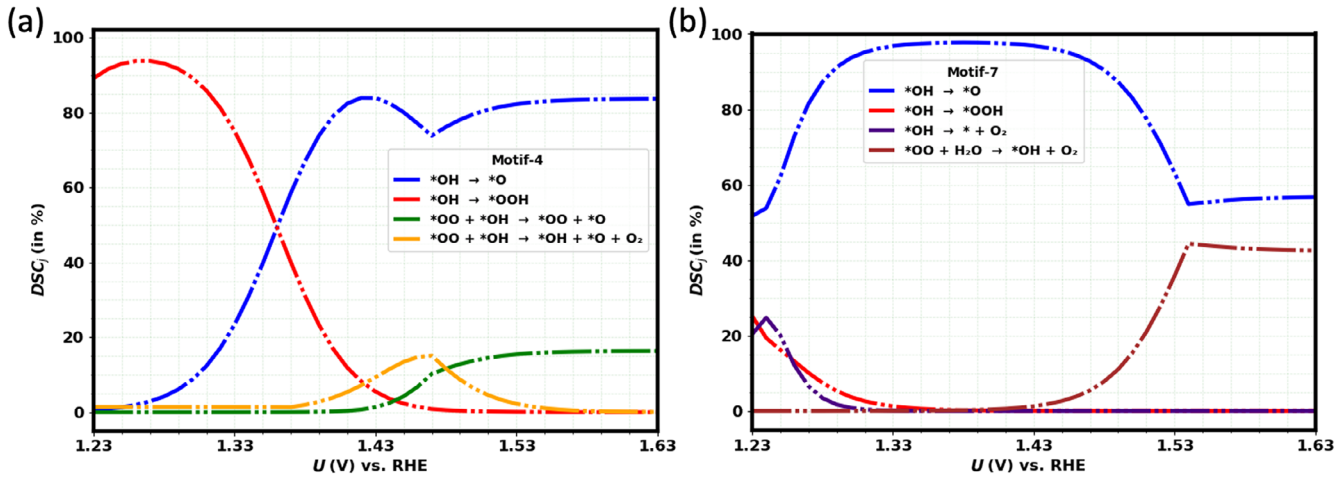

Figure 5. Potential-dependent degree of span control (DSC_j) for the elementary steps of the OER on the octahedral motifs of Co_3O_4(001) (see Figure 1): a) **Motif-4**, b) **Motif-7**. Contributions below 5% are excluded for clarity. The analysis reveals that the main limiting steps across the different octahedral motifs include *OH → *O, *O → *OOH, and *OO + *OH → *OH + *O + O_2, highlighting the critical role of *OH oxidation, O—O bond formation, and O_2 desorption through a Walden-like step in the OER, respectively.

potentials, which is in agreement with the other two tetrahedral motifs.

Figure 4 shows the DSC plots for the pseudo-octahedral motifs (**Motif-5–6**). Unlike the tetrahedral case, the main kinetic bottleneck in **Motif-5** refers to the desorption of molecular oxygen (cf. Figure 4a). The desorption of O_2 is achieved by a Walden-type step,[10,41,64,65] in which the active Co site—after bond cleavage—is directly covered by an incoming water molecule to form an *OH group. This finding underlines the importance of concerted desorption-adsorption steps to the description of electrocatalytic processes, emphasizing that Walden-type mechanisms excel traditional pathways for the pseudo-octahedral motif (cf. Figure S8 in Section S5). A similar finding was recently reported for the OER on IrO_2(110).[66] In contrast, the DSC_j plot for **Motif-6** clearly differs from **Motif-5** in terms of the limiting step, which is related to the oxidation of the *OH intermediate in the entire potential regime (cf. Figure 4b). We recall that **Motif-6** consists of a pseudo-octahedral Co site as active site and a neighboring octahedral Co site as auxiliary site (cf. Figure 1), and the oxidation of the *OH intermediate takes place on the octahedral auxiliary site in the realm of a bifunctional mechanism (cf. Figure S8). Therefore, we conclude that the electrocatalytic activity of the pseudo-octahedral main active site is determined by the Walden-type desorption of O_2, which is not seen in Figure 4b because the contribution of the octahedral auxiliary site to the current density exceeds that of the pseudo-octahedral Co site.

The octahedral motifs (**Motif-4** and **Motif-7**, cf. Figure 5) exhibit a different limitation in the formation of molecular oxygen. In this case, the DSC analysis reveals that deprotonation of *OH to *O is the dominant step determining the reaction rate at relevant OER potentials. While the formation of the *OOH adsor-

bate is identified as the main limitation for **Motif-4** at $U < 1.35$ V versus RHE, the *OH-to-*O step gradually becomes more important and reaches a contribution of up to 80% to the reaction rate at $U > 1.50$ V versus RHE. In **Motif-7**, the oxidation of the *OH adsorbate contributes up to 100% to the reaction rate, while the O_2 desorption step via a Walden step reaches a contribution of about 40% at $U > 1.55$ V versus RHE. Nevertheless, the *OH-to-*O step is the main kinetic constraint for the octahedral motifs, and this finding is consistent with the fact that the elementary steps at the octahedral auxiliary sites of tetrahedral or pseudo-octahedral sites are also limited by the oxidation of the *OH adsorbate (cf. Figures 3c and 4b).

In summary, our comparative analysis demonstrates that, while all different site types (tetrahedral, pseudo-octahedral, and octahedral) contribute to OER activity to a certain extent, they clearly differ in their mechanistic constraints, ranging from O—O bond formation to O_2 desorption and surface oxidation of *OH. Furthermore, it should be noted that apart from the pseudo-octahedral sites, there is no single elementary reaction step that controls the reaction rate, but that several reaction steps contribute to the current density to varying degrees. This makes the optimization of the active sites on the surface of spinel Co_3O_4 a challenging but equally rewarding task, since—in addition to changes in the local environment of active sites—one has to consider that there is an ensemble of active sites consisting of different sites with different coordination and different limit steps, all of which require dissimilar optimization.

4. Conclusion

In the present work, we investigate the oxygen evolution reaction (OER) at the A- and B-terminations of Co_3O_4(001) using a combination of density functional theory calculations and *ab initio* molecular dynamics simulations. Our theoretical analysis bridges the gap from changes in the local coordination under the formation of pseudo-octahedral sites to a dedicated analysis of the elementary steps of the OER, which is performed by a descriptor-based analysis using the $G_{max}(U)$ descriptor. This allows us to monitor the contribution of the elementary reaction steps to the reaction rate through the concept of degree of span control (DSC) for each active site motif to elucidate structure–activity relationships that determine catalytic performance under OER conditions.

Three main types of active sites were identified on the hydroxylated surfaces of the A- and B-terminations of Co_3O_4(001) under anodic polarization, exhibiting tetrahedral, octahedral, or pseudo-octahedral coordination of cobalt. While the octahedral and pseudo-octahedral sites are somewhat more catalytically active than the tetrahedral sites in the OER, there is agreement that the limiting reaction steps for these active site motifs are systematically different: formation of the O—O bond, desorption of the product O_2, and surface oxidation of *OH groups to form the *O intermediate are identified as the main limitation for the tetrahedral, pseudo-octahedral, and octahedral sites, respectively.

The reported trends in OER activity and limiting steps of the different active sites can contribute to the development of improved spinel-based catalysts for OER and highlight that the optimization of complex oxide materials under electrochemical conditions requires the control of multiple parameters. On the one hand, control over subsurface tetrahedral sites is desirable, which can be activated by water-mediated transformation and increase the density of active sites on the Co_3O_4 surface. On the other hand, the optimization of Co_3O_4-based catalysts does not require focusing on a single active site, but rather treating the diversity of active sites with different coordination as an ensemble of active sites with different mechanistic implications, as exploited by the structure-activity relationships described in this work. While we have modeled each motif independently using a static DFT framework, it is conceivable that, under reaction conditions, intermediates may migrate across adjacent motifs, allowing different reaction steps to proceed at different local environments. This ensemble-level reactivity, supported by AIMD simulations and experimental evidence of surface transformation, offers a promising direction for understanding and designing complex oxide catalysts under realistic OER conditions.

Acknowledgments

K.D., S.K., A.F., R.P., K.T., and K.S.E. acknowledge funding from the CRC/ TRR247: "Heterogeneous Oxidation Catalysis in the Liquid Phase" (Project number 388390466-TRR 247, projects A06, B04, and A09). K.T. and K.S.E. further acknowledge funding from the RESOLV Cluster of Excellence, funded by the Deutsche Forschungsgemeinschaft under Germany's Excellence Strategy–EXC 2033–390677874–RESOLV.

We acknowledge support by the Open Access Publication Fund of the University of Duisburg-Essen.

Open access funding enabled and organized by Projekt DEAL.

Conflict of Interests

The authors declare no conflict of interest.

Data Availability Statement

The data that support the findings of this study are available in the Supporting Information of this article.

Keywords: Co_3O_4 · Degree of span control · Descriptor approach · Octahedral site · Oxygen evolution reaction · Pseudo-octahedral site · Tetrahedral site

[1] T. Reier, M. Oezaslan, P. Strasser, *ACS Catal.* **2012**, *2* 1765–1772.
[2] N. Govindarajan, G. Kastlunger, H. H. Heenen, K. Chan, *Chem. Sci.* **2022**, *13* 14–26.

[3] G. Kastlunger, P. Lindgren, A. A. Peterson, *J. Phys. Chem. C* **2018**, *122*, 12771–12781.
[4] E. Tayyebi, Y. Abghoui, E. Skúlason, *ACS Catal.* **2019**, *9*, 11137–11145.
[5] N. Abidi, S. N. Steinmann *Curr. Opin. Electrochem.* **2022**, *33*, 100940.
[6] Y. Peng, H. Hajiyani, R. Pentcheva, *ACS Catal.* **2021**, *11*, 5601–5613.
[7] M. Bajdich, M. García-Mota, A. Vojvodic, J. K. Nørskov, A. T. Bell, *J. Am. Chem. Soc.* **2013**, *135*, 13521–13530.
[8] M. García-Mota, M. Bajdich, V. Viswanathan, A. Vojvodic, A. T. Bell, J. K. Nørskov, *J. Phys. Chem. C* **2012**, *116*, 21077–21082.
[9] K. Bhattacharyya, A. A. Auer, *J. Phys. Chem. C* **2022**, *126* 18623–18635.
[10] S. Razzaq, S. Faridi, S. Kenmoe, M. Usama, D. Singh, L. Meng, F. Vines, F. Illas, K. S. Exner, *J. Am. Chem. Soc.* **2025**, *147*, 161–168.
[11] K. Dhaka, K. S. Exner, *J. Catal.* **2025**, *443*, 115970.
[12] M. Sokolov, K. S. Exner *Chem. Catalysis* **2024**, *4*, 101039.
[13] S. Razzaq, K. S Exner. M. S. b. t. D., *ACS Catal.* **2023**, *13*, 1740–1758.
[14] K. S. Exner, *ACS Catal.* **2020**, *10*, 12607–12617.
[15] Z. Liu, H. M. A. Amin, Y. Peng, M. Corva, R. Pentcheva, K. Tschulik, *Adv. Funct. Mater.* **2023**, *33*, 2210945.
[16] M. Yu, F. Waag, C. K. Chan, C. Weidenthaler, S. Barcikowski, H. Tüysüz, *ChemSusChem* **2020**, *13*, 520–528.
[17] C. Qiu, F. Maroun, M. Bouvier, I. Pacheco, P. Allongue, T. Wiegmann, C. Hendric Scharf, V. de Manuel-Gonzalez, F. Reikowski, J. Stettner, O. M. Magnussen, *ChemCatChem* **2024**, *16*, e202400988.
[18] J. Timoshenko, F. T. Haase, S. Saddeler, M. Rüscher, H. S. Jeon, A. Herzog, U. Hejral, A. Bergmann, S. Schulz, B. Roldan Cuenya, *J. Am. Chem. Soc.* **2023**, *145*, 4065–4080.
[19] Y. Zhou, S. Sun, C. Wei, Y. Sun, P. Xi, Z. Feng, Z. J. Xu, *Adv. Mater.* **2019**, *31*, 1902509.
[20] T. Wiegmann, I. Pacheco, F. Reikowski, J. Stettner, C. Qiu, M. Bouvier, M. Bertram, F. Faisal, O. Brummel, J. Libuda, J. Drnec, P. Allongue, F. Maroun, O. M. Magnussen, *ACS Catal.* **2022**, *12*, 3256–3268.
[21] H. Jiang, Q. He, Y. Zhang, L. Song, *Acc. Chem. Res.* **2018**, *51*, 2968–2977.
[22] B. He, F. Bai, P. Jain, T. Li, *Small* **2025**, *21*, 2411479.
[23] H. Komiya, K. Obata, O. Sekizawa, K. Nitta, K. Xu, M. Wada, K. Takanabe, *Angew. Chem., Int. Ed.* **2025**, *64*, e202501579.
[24] M. G. Ahmed, Y. F. Tay, X. Chi, A. S. Razeen, Y. Fang, M. Zhang, A. Sng, S. Y. Chiam, A. Rusydi, L. H. Wong, *Angew. Chem., Int. Ed.* **2025**, *64*, e202416757.
[25] T. Kox, S. Kenmoe, *Dalton Trans.* **2024**, *53*, 13184–13194.
[26] F. B. S. Nkou, S. Kenmoe, *ChemCatChem* **2025**, *17*, e202401885.
[27] D. H. Douma, K. N. Nono, A. H. Omranpoor, A. Lamperti, A. Debernardi, S. Kenmoe, *J. Phys. Chem. C* **2023**, *127*, 5351–5357.
[28] A. H. Omranpoor, A. Bera, D. Bullert, M. Linke, S. Salamon, S. Webers, H. Wende, E. Hasselbrink, E. Spohr, S. Kenmoe, *J. Chem. Phys.* **2023**, *158*, 164703.
[29] Y. Kang, F. Zhang, B. Liu, Y. Sun, X. Zhang, W. Song, Y. Wei, Z. Zhao, J. Liu, *Phys. Chem. Chem. Phys.* **2020**, *22*, 18672–18680.
[30] A. Bergmann, E. Martinez-Moreno, D. Teschner, P. Chernev, M. Gliech, J. F. de Araújo, T. Reier, H. Dau, P. Strasser, *Nat. Commun.* **2015**, *6*, 8625.
[31] F. Reikowski, F. Maroun, I. Pacheco, T. Wiegmann, P. Allongue, J. Stettner, O. M. Magnussen, *ACS Catal.* **2019**, *9*, 3811–3821.
[32] G. Kresse, J. Hafner, *Phys. Rev. B* **1993**, *48*, 13115–13118.
[33] G. Kresse, J. Furthmüller, *Comput. Mater. Sci.* **1996**, *6*, 15–50.
[34] G. Kresse, J. Furthmüller, *Phys. Rev. B* **1996**, *54*, 11169–11186.
[35] K. Mathew, R. Sundararaman, K. Letchworth-Weaver, T. A. Arias, R. G. Hennig, *J. Chem. Phys.* **2014**, *140*, 084106.
[36] L. Xu, Q. Jiang, Z. Xiao, X. Li, J. Huo, S. Wang, L. Dai, *Angew. Chem., Int. Ed.* **2016**, *55*, 5277–5281.
[37] T. Quast, H. B. Aiyappa, S. Saddeler, P. Wilde, Y. Chen, S. Schulz, W. Schuhmann, *Angew. Chem., Int. Ed.* **2021**, *60*, 3576–3580.
[38] E. M. Davis, A. Bergmann, H. Kuhlenbeck, B. Roldan Cuenya, *J. Am. Chem. Soc.* **2024**, *146*, 13770–13782.
[39] S. Pan, H. Li, T. Wang, Y. Fu, S. Wang, Z. Xie, L. Wei, H. Li, N. Li, *ACS Catal.* **2024**, *14*, 13814–13824.
[40] F. Hess, H. Over, *ACS Catal.* **2023**, *13*, 3433–3443.
[41] K. S. Exner, *Adv. Sci.* **2023**, *10*, 2305505.
[42] S. Yu, Z. Levell, Z. Jiang, X. Zhao, Y. Liu, *J. Am. Chem. Soc.* **2023**, *145*, 25352–25356.
[43] J. K. Nørskov, J. Rossmeisl, A. Logadottir, L. Lindqvist, J. R. Kitchin, T. Bligaard, H. Jónsson, *J. Phys. Chem. B* **2004**, *108*, 17886–17892.
[44] H. Hajiyani, R. Pentcheva, *ACS Catal.* **2018**, *8*, 11773–11782.
[45] T. Kox, E. Spohr, S. Kenmoe, *Front. Energy Res.* **2020**, *8*, 604799.
[46] P. W. Menezes, A. Indra, A. Bergmann, P. Chernev, C. Walter, H. Dau, P. Strasser, M. Driess, *J. Mater. Chem. A Mater.* **2016**, *4*, 10014–10022.
[47] F. T. Haase, A. Bergmann, T. E. Jones, J. Timoshenko, A. Herzog, H. S. Jeon, C. Rettenmaier, B. R. Cuenya, *Nat. Energy* **2022**, *7*, 765–773.
[48] S. Kozuch, S. Shaik, *Acc. Chem. Res.* **2011**, *44*, 101–110.
[49] Y. Huang, R. J. Nielsen, W. A. Goddard, *J. Am. Chem. Soc.* **2018**, *140*, 16773–16782.
[50] M. Vasanthapandiyan, S. Singh, F. Bononi, O. Andreussi, N. Karmodak, *J. Chem. Phys.* **2023**, *159*, 111001.
[51] H. H. Pham, M.-J. Cheng, H. Frei, L.-W. Wang, *ACS Catal.* **2016**, *6*, 5610–5617.
[52] C. C. L. McCrory, S. Jung, I. M. Ferrer, S. M. Chatman, J. C. Peters, T. F. Jaramillo, *J. Am. Chem. Soc.* **2015**, *137*, 4347–4357.
[53] J. Huang, X. Zhu, M. Eikerling, *Electrochim. Acta* **2021**, *393*, 139019.
[54] F. Calle-Vallejo, M. T. M. Koper, *Electrochim. Acta* **2012**, *84*, 3–11.
[55] C. F. Dickens, C. Kirk, J. K. Nørskov, *J. Phys. Chem. C* **2019**, *123*, 18960–18977.
[56] H. N. Nong, L. J. Falling, A. Bergmann, M. Klingenhof, H. P. Tran, C. Spöri, R. Mom, J. Timoshenko, G. Zichittella, A. Knop-Gericke, S. Piccinin, J. Pérez-Ramírez, B. R. Cuenya, R. Schlögl, P. Strasser, D. Teschner, T. E. Jones, *Nature* **2020**, *587*, 408–413.
[57] A. Baz, S. T. Dix, A. Holewinski, S. Linic, *J. Catal.* **2021**, *404*, 864–872.
[58] A. Baz, A. Holewinski, *J. Catal.* **2021**, *397*, 233–244.
[59] K. S. Exner, *J. Energy Chem.* **2023**, *83*, 247–254.
[60] C. T. Campbell, *ACS Catal.* **2017**, *7* 2770–2779.
[61] C. Stegelmann, A. Andreasen, C. T. Campbell, *J. Am. Chem. Soc.* **2009**, *131*, 8077–8082.
[62] T. Binninger, M.-L. Doublet, *Energy Environ. Sci.* **2022**, *15*, 2519–2528.
[63] T. Mou, D. A. Bushiri, D. V. Esposito, J. G. Chen, P. Liu, *Angew. Chem., Int. Ed.* **2024**, *63*, e202409526.
[64] T. Liu, Y. Zhao, T. Zhai *J. Am. Chem. Soc.* **2024**, *146*, 6461–6465.
[65] S. Faridi, S. Razzaq, D. Singh, L. Meng, F. Viñes, F. Illas, K. S. Exner, *J. Mater. Chem. A Mater.* **2025**, *13*, 16481–16490.
[66] M. Usama, S. Razzaq, C. Hättig, S. N. Steinmann, K. S. Exner, *Nat. Commun.* **2025**, *16*, 6137.

Manuscript received: June 18, 2025
Revised manuscript received: July 31, 2025
Accepted manuscript online: August 12, 2025
Version of record online: September 3, 2025